Lattice distortion and electronic structure of BaAg_{2}As_{2} across its nonmagnetic phase transition

X. Lou, H. C. Xu, C. H. P. Wen, T. L. Yu, W. Z. Wei, Q. Yao, Y. H. Song, Eve Emmanouilidou, Bing Shen, N. Ni, P. Dudin, Y. B. Huang, J. Denlinger, R. Sutarto, W. Li, R. Peng, and D. L. Feng

Phys. Rev. B **101**, 075123 — Published 18 February 2020

DOI: 10.1103/PhysRevB.101.075123

Lattice distortion and electronic structure of $BaAg_2As_2$ across its non-magnetic phase transition

X. Lou,[1] H. C. Xu,[1] C. H. P. Wen,[1] T. L. Yu,[1] W. Z. Wei,[1] Q. Yao,[1] Y. H. Song,[1] Eve Emmanouilidou,[2] Bing Shen,[2] N. Ni,[2] P. Dudin,[3] Y. B. Huang,[4] J. Denlinger,[5] R. Sutarto,[6] W. Li,[1,7] R. Peng,[1,*] and D. L. Feng[1,7,8]

[1]*Advanced Materials Laboratory, State Key Laboratory of Surface Physics, and Department of Physics, Fudan University, Shanghai 200433, China*
[2]*Department of Physics and Astronomy and California NanoSystems Institute, University of California, Los Angeles, CA 90095, USA*
[3]*Diamond Light Source, Harwell Science and Innovation Campus, Didcot OX11 0DE, United Kingdom*
[4]*Shanghai Institute of Applied Physics, Chinese Academy of Sciences, Shanghai 201204, China*
[5]*Advanced Light Source, Lawrence Berkeley National Laboratory, Berkeley, CA 94720, USA.*
[6]*Canadian Light Source, Saskatoon, Saskatchewan, S7N 2V3, Canada*
[7]*Collaborative Innovation Center of Advanced Microstructures, Nanjing 210093, China*
[8]*Hefei National Laboratory for Physical Science at Microscale, CAS Center for Excellence in Quantum Information and Quantum Physics, and Department of Physics, University of Science and Technology of China, Hefei 230026*

(Dated: February 4, 2020)

$BaAg_2As_2$, a sibling compound of $BaFe_2As_2$ with a non-magnetic phase transition around 150 K, is studied by the comprehensive measurements of angle-resolved photoemission spectroscopy, synchrotron x-ray diffraction and resonant soft x-ray scattering. The Fermi surfaces and electronic structure of $BaAg_2As_2$ are revealed, with strong k_z dispersion, consistent with the strongly contracted c/a ratio in $BaAg_2As_2$. Across the phase transition, splitting of [101] Bragg peak is observed, showing a structural distortion with the in-plane distortion magnitude $\delta = |a - b|/(a + b) = 0.0052$. Although the nesting condition is satisfied in some parallel Fermi surface sectors, there is no signature of charge density wave order at the nesting wave vector. Moreover, neither a charge density wave gap opening nor band reconstruction are observed across the phase transition. Instead, an enhancement on the spectral weight of dispersive bands is observed across the structural phase transition, which can explain the sharp drop of resistivity below the phase transition temperature. These studies could enrich the understanding of the variable and common features of the structural transition in transition metal pnictide layered materials.

INTRODUCTION

Two-dimensional layers made of transition metal cations (TM) and pnictide anions (Pn) provide a rich playground for novel physical phenomena and various phase transitions, such as the structural phase transition [1], magnetism [2, 3], the charge density wave (CDW) order [4, 5] and superconductivity [4–6], etc. In doped $BaFe_2As_2$, a prototypical Fe-pnictide superconductor, the high temperature superconducting phase happens in the vicinity of a collinear antiferromagnetic order and a tetragonal-orthorhombic structural distortion. The low-energy electronic structure reconstructs at the structural transition temperature, with different orbitals splitting at an energy scale much larger than the hopping integral varied by the structural distortion [7, 8], demonstrating an electronically driven nematic transition relating with orbital/spin order, which has ignited intensive researches [9]. On the other hand, the structural distortion also happens in other TM-Pn layered materials sibling to $BaFe_2As_2$. However, the underlying driving force has been shown to be different, such as a pure lattice-driven distortion in $BaNi_2As_2$ [6], and CDW-order-driven distortions in $BaPt_2As_2$ and $SrPt_2As_2$ [4, 5].

Recently, materials containing AgAs layers including $BaAg_2As_2$ [10], $SrAg_4As_2$ and $EuAg_4As_2$ [11, 12] have been synthesized, with a common resistivity anomaly above 100 K [10, 11]. Considering the absence of magnetism-active species, the nature of the phase transition was speculated to be a nonmagnetic phase transition, particularly a structural distortion [12]. Theoretical calculations have pointed out the possibility of an electronic instability. However, so far the nature of this phase transition has not been identified experimentally. The details of the distorted structure in $BaAg_2As_2$ were not resolved by previous x-ray diffraction (XRD) studies [10]. Moreover, it remains unknown whether the transition is related to any electronic instability, such as the orbital order, or the CDW formation under Fermi surface nesting. Resolving the crystal and electronic structure of $BaAg_2As_2$ and their variations across the phase transition would be a vital step towards understanding the novel properties in AgAs layered compounds. Moreover, it would facilitate the understanding of the variable and common features of the structural transition in TM-Pn layered materials.

Here we report a systematic study of the electronic structure and the phase transition in $BaAg_2As_2$ using synchrotron XRD, angle-resolved photoemission spectroscopy (ARPES) and resonant soft x-ray scattering (RSXS). At the transition temperature, a structural distortion is observed, and the in-plane distortion magnitude is estimated to be $\delta = |a - b|/(a + b) = 0.0052$, similar to what has been observed in $BaFe_2As_2$[1]. Three dimensional(3D) electronic structure is revealed, with stronger dispersion along the k_z direction than that in $BaFe_2As_2$. The three dimensional nature of the electronic structure is consistent with the homoatomic As-As bonding along the c direction [10].However, with the structural transition, there is no band splitting or Fermi surface reconstruction in $BaAg_2As_2$, which is in contrast to Fe-based

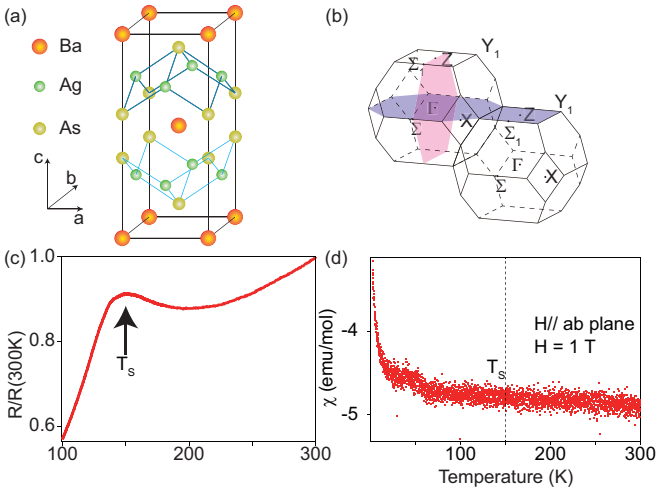

FIG. 1: (a) Illustration of crystallographic structure of $BaAg_2As_2$ at room temperature. (b) Sketch of Brillouin Zones (BZs) of $BaAg_2As_2$. The red and blue shadows illustrate the momentum space sampled in Fig. 3(a) and Fig. 3(b), respectively. (c) Temperature dependence of the electrical resistivity of $BaAg_2As_2$ on a copper holder from 100 K to 300 K. (d) Temperature-dependent magnetic susceptibility of $BaAg_2As_2$ measured with $B \parallel$ ab at $B = 1$ T.

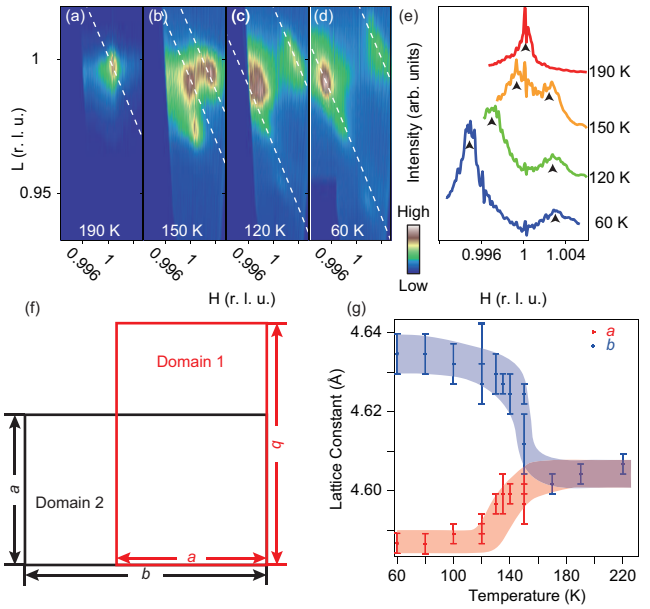

FIG. 2: (a)-(d) Reciprocal space intensity map of $BaAg_2As_2$ taken around the $[HKL] = [101]$ Bragg Peak at different temperatures from 190 K to 60 K with photon energies 1480 eV. The dashed lines represent domain rings. (e) Intensity distribution curve along L=1 corresponding to (a)-(d). (f) Sketch of two different domains after a tetragonal-to-orthorhombic phase transition. (g) Evolution of lattice constants as a function of temperature across the phase transition. Above 150 K, the lattice constant a is equal to b. The error bars are determined by the size of the diffraction spots.

superconductors. Although the Fermi surfaces show possible nesting conditions, there is no gap opening at the Fermi energy close to these momenta, and RSXS measurements find no CDW orders at the possible nesting wave vectors. Temperature-dependent ARPES studies resolve an enhancement of the spectral weight in the dispersive features across the structural phase transition, which can be related to the sharp drop of electrical resistivity.

EXPERIMENTAL AND SAMPLE CHARACTERIZATION

Single crystals of $BaAg_2As_2$ were grown with the flux method, using AgAs as the flux. At room temperature, $BaAg_2As_2$ possesses a body-centered $ThCr_2Si_2$-type structure [Fig. 1(a)], and its three dimensional Brillouin zone (BZ) in reciprocal lattice is shown in Fig. 1(b). The composition of our samples is determined to be $Ba_{1.01\pm0.05}Ag_{1.92\pm0.06}As_{2.00\pm0.04}$ using an electron probe microanalyzer (EPMA). The Ag is slightly deficient in our samples, while this off-stoichiometry is much less than that in a previous report (~24% Ag deficiency through energy dispersive x-ray analysis) [10].

The temperature-dependent electrical resistivity of $BaAg_2As_2$ was measured by a Quantum Design Physical Property Measurement System (PPMS). As the temperature decreases, the resistivity first shows a metallic behaviour and then increases from 200 K to 151 K [Fig. 1(c)]. After that, the resistivity decreases more sharply. The transition temperature (151 K) is lower than that in a previous report (175 K) [10], which may be related to the reduced deficiency of Ag in our samples. We have also conducted resistivity measurements on 10 more different sample, and all the samples show the phase transition with the transition temperatures of 146±6 K (see Supplementary Fig. S1 [13]). For rigidity of the combined studies, the electrical resistivity measurement [Fig. 1(c)] and temperature dependent ARPES measurements [Fig. 7] were performed on the same samples.

The temperature-dependent magnetic susceptibility of $BaAg_2As_2$ was measured using a Quantum Design Superconducting Quantum Interference Device (SQUID), and was found to be negative in the entire temperature range, indicating a diamagnetic behaviour [Fig. 1(d)]. An upturn of magnetic susceptibility is observed at low temperature, which is similar to that of $SrAg_4As_2$ [11] and $SrCu_2As_2$ [14], possibly coming from the trace amount of paramagnetic impurity in the samples [14]. The diamagnetic nature and the absence of strong magnetic response at T_s suggest that the phase transition in $BaAg_2As_2$ is not related to magnetism.

ARPES data were collected at Beamline I05 of Diamond Light Source (with the overall energy resolution of 5~12 meV, the endstation pressure $\leq 1.5\times10^{-10}$ mbar), Beamline 4.0.3 of Advanced Light Source (ALS) (the overall energy resolution of 12 meV, the endstation pressure $\leq 5\times10^{-11}$ mbar), and Beamline 09U of Shanghai Synchrotron Radiation Facility (SSRF) (the overall energy resolution of 20 meV, the endstation pressure $\leq 6.3\times10^{-11}$ mbar). We found that the sample is easy to be cleaved perpendicular to c axis to get a flat

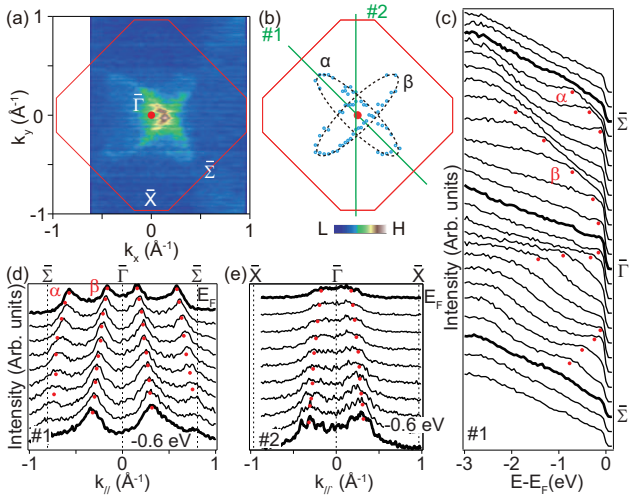

FIG. 3: (a) In-plane photoemission intensity map through the BZ center Γ (near the blue cross-section in Fig. 1(c)) from integrating the spectra over [E_F - 20 meV, E_F +2 0 meV]. The photon energy used is 105 eV. (b) Fermi crossings (blue circles) determined by photoemission data in (a). (c) Energy distribution curves (EDCs) along momentum cut #1 in (b). (d) Momentum distribution curves (MDCs) along momentum cut #1 in (b). (e) MDCs along momentum cut #2 in (b). All data were taken with *p* polarization.

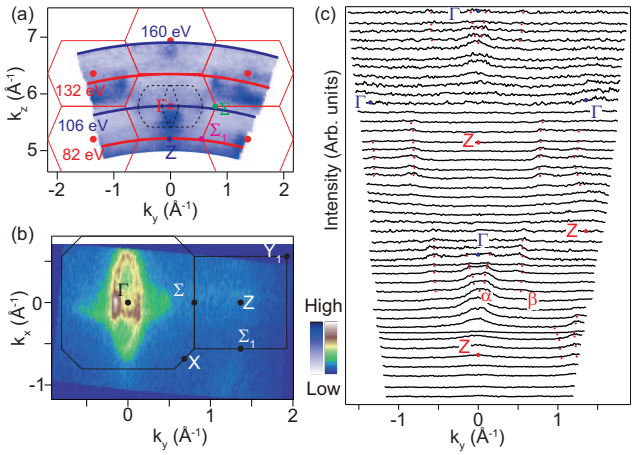

FIG. 4: (a) Photon energy dependent photoemission intensity map in Γ-Σ-Σ_1-Z plane (the red cross-section in Fig 1(b)). The Fermi surfaces are indicated by dashed lines. (b) Photoemission intensity map taken using 105 eV photons, and the corresponding location of the momentum space is illustrated by the blue cross-section in the three dimensional BZ in Fig 1(b). The maps are integrated over [E_F - 20 meV, E_F + 20 meV]. (c) MDCs at E_F along the k$_y$ direction shown in panel (a) measured at different photon energies. The inner potential is set to be 26 eV.

surface for ARPES measurement. Considering that the crystal structure and its hardness are similar to Fe-based 122 systems, the cleavage should happen at adjacent alkaline-earth planes, and each side of the cleaved plane has the same amount of alkaline-earth atoms similar to other 122 based materials without charge redistribution [15].

Synchrotron XRD and RSXS measurements were performed at the REIXS 10ID-2 beamline of the Canadian Light Source (CLS) with elliptically polarized undulator (EPU) covering an energy range of 80~2000 eV. The energy resolution is $\triangle E/E = 10^{-4}$ at 1000 eV. The spot size is ~250 μm × 150 μm. The data were collected by a microchannel plate (MCP) with a resistive anode encoder detector. The MCP diameter is 25 mm and the MCP image is collected in 128 × 128 pixels. The pressure of the endstation was kept under 6.7×10^{-10} mbar during scattering measurements.

TEMPERATURE DEPENDENT XRD STUDIES

To study the possible structural transition, temperature-dependent XRD scans on [*HKL*] = [101] reflections were performed using 1480 eV photons. Note that the photon energy we used here was much lower than 17459 eV in previous XRD measurements on $BaAg_2As_2$ [10], which could significantly enhance the momentum resolution. The [101] diffraction shows a single peak above the transition temperature [Fig. 2(a)]. As the temperature decreases, the [101] peak splits along *H* at 150 K [Fig. 2(b)- 2(d)], consistent with the transition temperature observed in resistivity measurements. The split [101] peaks broaden along circular curves centered at [000], indicating rotating domains that may be caused by stress-induced sample cracking. The third peak with lower *L* at 150 K [Fig. 2(b)] does not fit the ring of rotating domains, and is absent at other temperatures. Its origin is unknown and could be related to some intermediate phases during the phase transition. The splitting of the [101] peak along *H* can be understood as an $a \neq b$ in-plane structural distortion as illustrated in Fig. 2(f). When the structural distortion happens, two kinds of domains with perpendicular in-plane orientations both contribute to the diffraction intensity, thus leading to the two peaks corresponding to *H* along *a* and *b*, respectively.

Based on the intensity distribution curves along L=1 as shown in Fig. 2(e), quantitative analysis of the lattice constants *a* and *b* is performed, and summarized in Fig. 2(g). Peak splitting happens at $T_s \approx 150$ K. At 60 K, *a* is decreased by 0.345% while *b* is increased by 0.701%. We can thus calculate the lattice distortion $\delta = |a - b|/(a + b) \approx 0.0052$. This value is comparable to that of $BaFe_2As_2$ ($\delta \approx 10^{-3}$) [2].

ELECTRONIC STRUCTURE

Structural transitions in $ThCr_2Si_2$ systems are usually accompanied by transitions in density wave orders such as spin density wave (SDW) [1] and CDW [4, 5]. An electron-instability-induced structural distortion has been speculated in $BaAg_2As_2$ by previous theoretical calculations [10] while lacking experimental evidence. To check and understand the possible electron-instability-induced phase transition, we studied the electronic structure of $BaAg_2As_2$ by ARPES. Figure 3 shows the measured in-plane band structure and Fermi

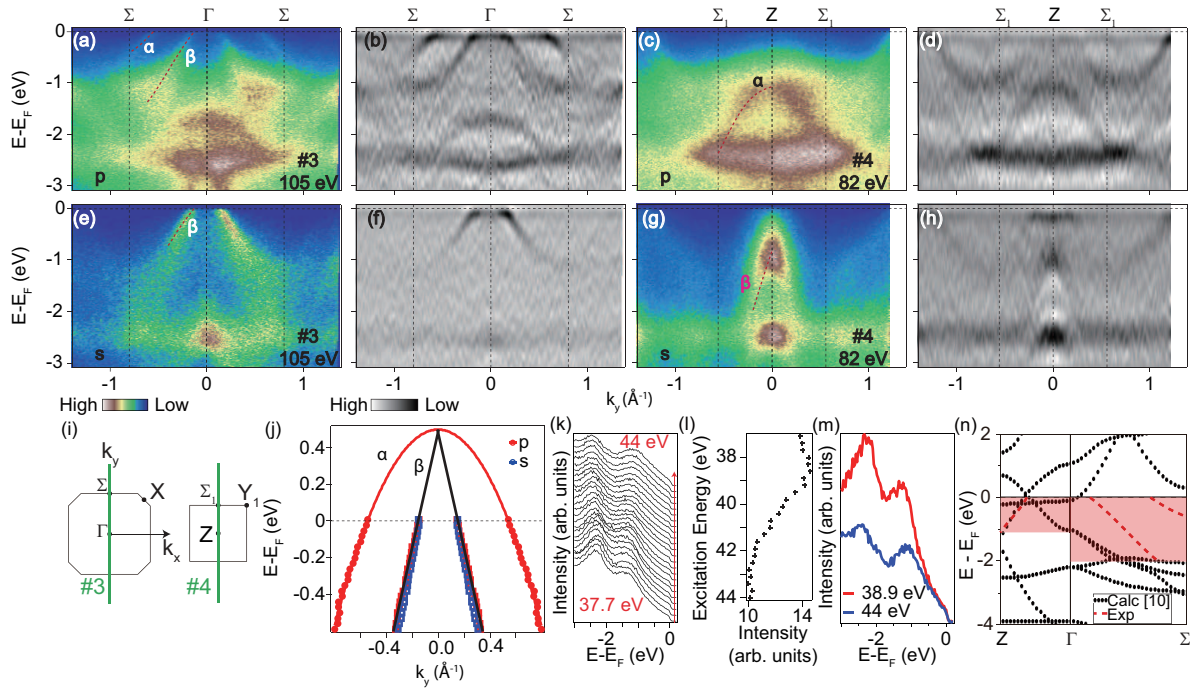

FIG. 5: (a) Photoemission intensity taken with p polarization along Σ-Γ-Σ (cut #3 in panel (i)). (b) Second derivative image of (a). (c) Photoemission intensity taken with p polarization along Σ_1-Z-Σ_1 (cut #4 in panel (i)). (d) Second derivative image of (d). (e)-(h) Same as (a)-(d) but taken with s polarization. (i) Sketch of in-plane BZs in Γ-X-Σ plane and Σ_1-Z-Y_1 plane, and the position of cut #3 and #4. (j) Band dispersion of α and β tracked by MDCs (cross symbols) and linear/parabolic fittings (solid lines). (k) Angle-integrated EDCs taken with 37.7 eV to 44 eV photons. (l) Integrated spectra intensity between -2 eV and -1 eV in (k) normalized by the incident photon flux. (m) A comparison of EDCs integrated over k_y = [-0.5 Å^{-1}, 0.5 Å^{-1}] taken with on-resonance (38.9 eV) and off-resonance (44 eV) photons. Both EDCs are normalized by the incident photon flux. (n) Comparison of band dispersion determined from ARPES experiments and from previous tight-binding linear muffin tin orbital band structure calculations [10]. The red shadows indicate the range of ARPES measurements.

surfaces of $BaAg_2As_2$. By tracking the spectral maxima at the Fermi energy [Fig. 3(a)], we found two elongated elliptical Fermi surfaces perpendicular to each other at the BZ center, denoted as α and β in Fig. 3(b). Along the high symmetric cut Γ-Σ (cut #1), both the energy distribution curves (EDCs) and momentum distribution curves (MDCs) show two hole-like bands (noted as α and β, correspondingly) crossing the Fermi level [Fig. 3(c)- 3(d)]. Along cut Γ-X (cut #2) through the crossing points of the two Fermi pockets, the bands α and β show no hybridization-induced splitting under the current experimental resolution [Fig. 3(e)].

To investigate the band dispersion along the k_z direction, ARPES studies with photon energies ranging from 74 to 160 eV were performed, covering about two BZs [Fig. 4(a)]. Variation of Fermi crossings at different photon energies can be clearly resolved. By assuming the inner potential to be 26 eV, the Fermi surfaces α and β match the period of the bulk 3D BZ well [Fig. 4(a)]. The periodicity of the 3D Fermi surfaces confirmed that the cleavage plane is perpendicular to the c axis of the crystals [Fig. 1(a)]. As shown in Fig. 4(b), there is no observable Fermi surface in the Z-Y_1-Σ_1 plane, contrast to that in the Γ-X-Σ plane [Fig. 4(b)], indicating strong k_z dependence of its electronic structure. Furthermore, MDCs at E_F show negligible features around the Z point, further indicating that all bands are below E_F at the Z-Y_1-Σ_1 plane. The band dispersion is more three dimensional than the isostructural $BaFe_2As_2$ [7], which is consistent with the significantly contracted c/a ratio and the strong homoatomic As-As bonding along the c direction in $BaAg_2As_2$ [10].

To avoid missing some bands in ARPES experiments due to matrix element effects, ARPES measurements were conducted with both p and s polarized photons. Along the Γ-Σ direction [Fig. 5(i)], two hole like bands can be observed using p polarized light [Fig. 5(a)], while only one hole like band can be observed using s polarized light [Fig. 5(e)]. By tracking the dispersion through fitting the corresponding MDCs, one can find that the dispersion of the inner hole bands measured using p polarized light coincides with the hole band measured using s polarized light, suggesting that both of them come from the β band. The dispersion of α band can be fitted well with parabolic curves in Fig. 5(j), with an effective mass of ~$2m_e$. Band β shows linear behavior deviating from parabolic dispersion, indicating a rather small effective mass [Fig. 5(j)]. Along the Z-Σ_1 direction, the top portions of the α and β bands are located around 1 eV below E_F in both polarisations [Figs. 5(c)- 5(h)]. There is weak spectral weight crossing the Fermi energy [Figs. 5(c) and 5(g)]. As shown in the second derivative spectra, these weak features near the Fermi

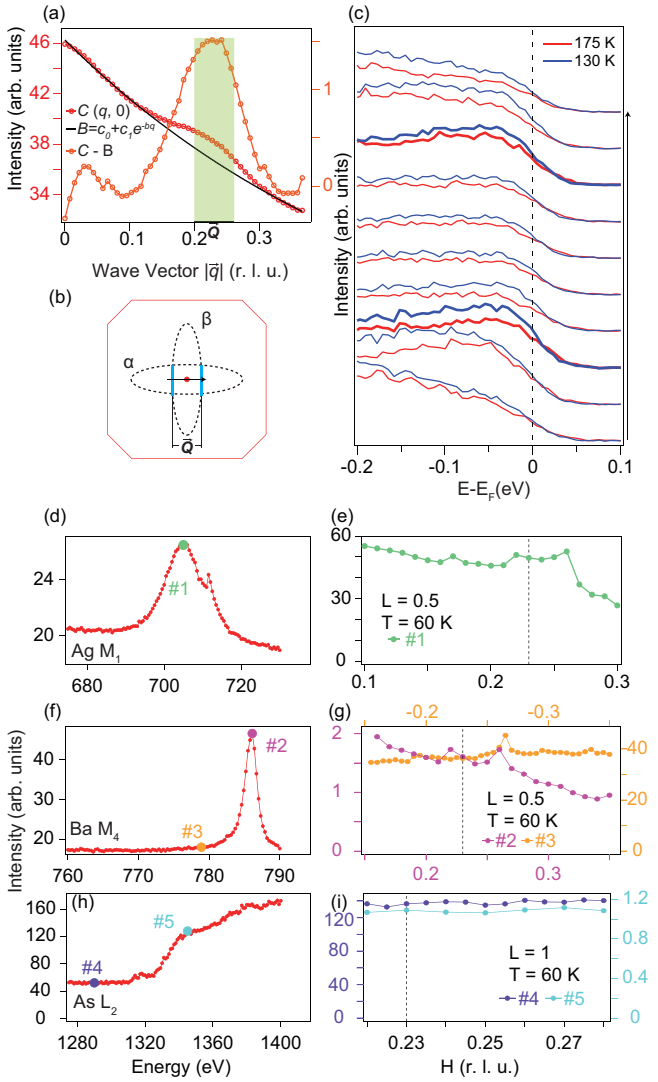

FIG. 6: (a) Auto-correlation of the ARPES spectral intensity near E_F at 203 K along the Γ-Σ direction. The black line is an exponential background. The subtracted result is presented as the orange line. (b) Sketch of the nesting wave vector Q determined in (a). (c) EDCs along the arrow marked in (b) showing no gap opening at low temperature. The EDCs at Fermi crossings are shown as thicker curves. (d) Ag M_1, (f) Ba M_4 and (h) As L_2 edge x-ray absorption spectroscopy curves. (e) [H 0 0.5] scans at a photon energy of 705 eV (green) as the same color noted in (d). (g) [H 0 0.5] scans at photon energies of 779 eV (orange) and 786 eV (magenta) as the same color noted in (f). (i) [H 0 1] scans at photon energies of 1290 eV (blue) and 1345 eV (pale blue) as the same color noted in (h). The H = 0.23 is indicated by dashed lines.

energy have dispersion identical to those in the Γ-X-Σ plane, which can be explained by k_z broadening due to poor k_z resolution in the ultraviolet photon energy range, while no Fermi surfaces are observed around the Z point. This confirms that the three-dimensional Fermi surfaces of $BaAg_2As_2$ consist of only hole pockets. Based on the measured Fermi surface volume and the Luttinger theorem [16], the carrier concentration in $BaAg_2As_2$ is estimated to be 0.17 ± 0.01 holes per unit cell. The ARPES results were reproduced on 5 samples measured at different beamlines (see Supplementary Fig. S2 and Table S1 for the measured Fermi surfaces and corresponding carrier concentration deduced based on Luttinger volume [13]). There is ±0.01 hole/u.c. difference in the doping level for different samples, which is the common uncertainty of the hole doping determined by ARPES. Therefore, even if different Ag vacancies have finite influence on the pocket size, it cannot account for all the hole concentration, indicating that the hole type carrier is intrinsic in $BaAg_2As_2$.

We investigated the valence band composition with 37.7 ~ 44 eV photons across the As 3d → 4p absorption edges [Fig. 5(k)]. The total spectral weight is integrated and normalized by the incident photon flux, showing a resonance enhancement at 38.9 eV [Fig. 5(l)]. Photoemission with 37.7 ~ 44 eV photons would give the band structure near the Z-Y_1-Σ_1 plane, thus the top parts of bands α and β are located around -1 eV. Comparing the on-resonant and off-resonant EDCs, the spectral weight corresponding to bands α and β is enhanced in the As 3d → 4p on-resonant data [Fig. 5(m)], suggesting significant As 4p orbital composition of these bands. This is consistent with previous XPS studies [10] which suggest valence formulations of $Ba^{2+}(Ag^{+})_2(As^{2-})_2$, and the 4p orbitals of As contributing to the major density of states (DOS) near Fermi energy.

TEMPERATURE DEPENDENT ARPES AND RXSX STUDIES

Magnetic susceptibility measurements suggest the absence of a magnetic transition [Fig. 1(d)], excluding the existence of spin related transitions. Nevertheless, the observed highly parallel Fermi surface sections suggest CDW as a possible candidate. The nesting condition of Fermi surfaces could cause an electronic instability such as the Peierls instability [17], which has been observed in typical CDW materials [18, 19]. From the measured Fermi surfaces of $BaAg_2As_2$, we determine the possible nesting vectors by their momentum-dependent autocorrelation [20–22]. The joint density of states,

$$C(\vec{q}, \omega) \equiv \int A(\vec{k}, \omega)A(\vec{k}+\vec{q}, \omega)d\vec{k}$$

is calculated in Fig. 6(a), where $A(\vec{k}, \omega)$ is the spectral function. After subtracting an exponential background, a peak is observed at $q_{\|}$ = 0.23 ± 0.03 as displayed in Fig. 6(a) , corresponding to the parallel Fermi surfaces sheet [Fig. 6(b)]. Therefore the CDW nesting vector could be $\vec{Q}$ = (0.23 ± 0.03, k, l) with arbitrary sliding along K or L. In the conventional scenario of a CDW transition, a CDW gap will open at the parallel Fermi surface sheets below the transition temperature [23, 24]. In contrast, by comparing the EDCs above and below the transition temperature along the cut marked in Fig. 6(b), there is no shift of leading edge at the Fermi crossings, suggesting the absence of a CDW gap [Fig. 6(c)]. Furthermore, not even a partial gap opening at non-dispersive spectral weights was observed, in contrast to the CDW gap opening observed in the Fermi patches in transition metal

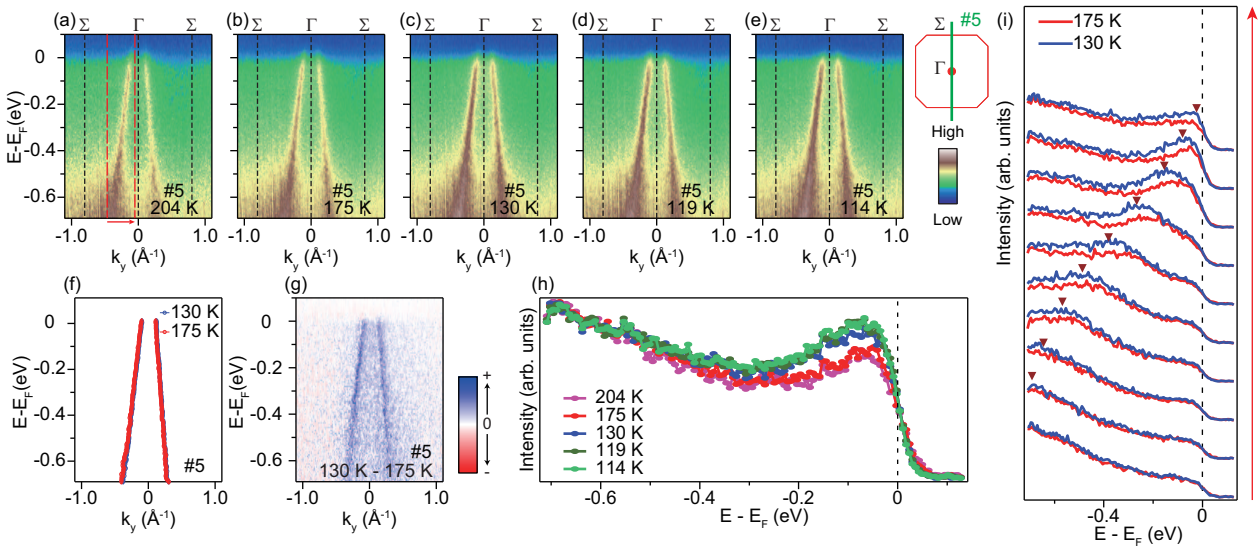

FIG. 7: (a)-(e) Photoemission spectra along Γ – Σ taken at 204 K~114 K. The right inset illustrates the position of cut #5.(f) Band dispersion extracted from MDCs at 130 K and 170 K. (g) Spectral weight difference between 175 K and 130 K. (h) EDCs taken at k_F of cut #5 at different temperatures. (i) Comparison of EDCs at 175 K and 130 K along the range of cut #5 marked by the red arrow in (a).

dichalcogenide materials [25]. Since the Fermi surfaces are contributed by the bulk bands with 3D dispersive characters [Fig. 4], the absence of gap opening excludes the existence of CDW in the bulk.

RSXS measurements were performed around the nesting wave vectors to further check the possible CDW order. Benefiting from its photon-in and photon-out process, RSXS has a deep penetration depth larger than tens of nanometers and has been used widely to detect the CDW order in the bulk [26]. By x-ray absorption spectroscopy measurements [Fig. 6(d), 6(f) and 6(h)], we select representative energies around Ag M1 edge (705 eV), Ba M4 edge (786 eV, 779 eV) and As L2 edge (1345 eV, 1290 eV), respectively. The scattering data collected at the resonant energies for all of the elements by MCP are near background level [Fig. 6(e), 6(g) and 6(i)], showing no CDW peak around H = 0.23 ± 0.03. Although a hump feature is observed at $\vec{Q}$ = (0.25, 0, 0.505) in both Figs. 6(e) and 6(g), we confirm that these peaks do not originate from CDW diffraction spots but from broad background features (Supplementary Fig. S3(a)-(d) [13]). Furthermore, this feature exists at both 240 K and 60 K (Supplementary Fig. S3(e) [13]), indicating that it is not relevant to the phase transition. Diffraction features were also investigated at fixed *H* by varying *L*, but CDW diffraction spots were not observed here either (Supplementary Fig. S4 [13]).

Although the conventional CDW transition is excluded in $BaAg_2As_2$, evolution in the electronic structure may provide vital information about the nature of this phase transition. In the photoemission spectra along Γ-Σ [Fig. 7(a)- 7(e)], no band structure reconstruction or splitting is observed, which is different from the drastic band reconstruction induced by the nematic order in Fe-based superconductors. Dispersion measured at 130 K exactly follows that measured at 175 K [Fig. 7(f)], indicating that the change of band dispersion is beyond our resolution. Intriguingly, the spectral weight of the dispersive part at 130 K is enhanced compared to that at 175 K while the background does not change [Fig. 7(g)]. A detailed comparison of EDCs at different temperatures indicates that the spectral weight enhancement happens mainly between 175 K and 130 K [Fig. 7(h)], consistent with the transition temperature from resistivity measurements. The enhancement of spectral weight can also be observed while comparing EDCs at different momenta in Fig. 7(i). According to Fig. 7(g) and 7(i) the increment of spectral weight happens within 0.6 eV, beyond the vicinity of the Fermi energy.

DISCUSSION

The band dispersion of $BaAg_2As_2$ along three dimensional momentum space is comprehensively revealed by ARPES. The bulk states show only hole-type Fermi surfaces in $BaAg_2As_2$, which is different from that of undoped $BaFe_2As_2$ with the coexistence of both electron and hole pockets and neutral charge [27]. The Hall coefficient measurements further indicate the hole-type carrier in $BaAg_2As_2$ bulk crystals (Supplementary Fig. S5 [13]). The difference in charge type between $BaAg_2As_2$ and $BaFe_2As_2$ can be explained by the different valence states and As-As bonding. Different from Fe^{2+} in $BaFe_2As_2$ which has 6 electrons of Fe 3d orbitals near Fermi energy, the Ag^+ in $BaAg_2As_2$ has full 4d shells and contributes little to Fermi surface. In contrast to the full shell of As^{3-} in $BaFe_2As_2$, the As^{2-} in $BaAg_2As_2$ would nominally have one hole at p orbital for each As. Considering that c parameter of $BaAg_2As_2$ is comparable to the collapsed phase of $CaFe_2As_2$ with even shorter As-As distance [10, 28, 29],

strong homoatomic As-As bonding happens in $BaAg_2As_2$ like in collapsed phase of $CaFe_2As_2$ [28]. The localized As-As bonding may reduce the itinerant hole carriers from 1 hole/As, which could explain the finite concentration of 0.17 holes per unit cell with As p orbitals in $BaAg_2As_2$.

The revealed band structure offer constraints to theoretical calculations of AgAs layered compounds. As shown in Fig. 5(n), the measured band dispersion along Γ-Σ and Γ-Z could not be reproduced by the current theoretical calculations in ref.10, which calls for future adjustment of theoretical calculations. The observed 3D electronic structure could be modulated by the truncation of the 3D crystal and broken As-As bond at the surface [30]. Nevertheless, we expect such modulation should be minor as our data do not fit any band splitting behavior of finite layers, but show even less bands than the calculation [10]. The deviation from the calculation could possibly relate with the fine structure of BaAg2As2, i.e. the accurate positions of atoms within each unit cell, are off in the previous report [10].

Considering the origin of the phase transition, our results do not support a CDW picture. In RSXS measurements, we did not find any transition-related diffraction peak at scattering vectors corresponding to Fermi surface nesting, which is typical in CDW materials [26]. A stronger evidence comes from the absence of either gap opening at the Fermi crossings, which is typical in conventional CDW materials [25], or the suppression of spectral weight at non-dispersive Fermi patches, which is usually the case in strongly correlated CDW materials[20, 25].

To understand the mechanism of the structural phase transition of $BaAg_2As_2$, it would be helpful to compare it with other TM-Pn layered materials as well. A small orthorhombicity appears quite clearly below 150K, which shows similar distortion magnitude in $BaFe_2As_2$ and is reminiscent of the nematic transition observed in iron pnictides, making it very intriguing to know whether it could have some similarity. In iron pnictides, the origin of the transition is electronically driven, relating with orbital/spin order [9], which induces a huge band splitting below the transition temperature. However, the significant band reconstruction relating with nematicity in Fe-based superconductors is absent in $BaAg_2As_2$ [Fig. 7]. To further compare the EDC at Fermi Crossing at different temperatures, we convolve the EDC at 130K with a Gaussian, which has a FWHM (full width at half maximum) of $3.5k_BT$ (k_B is the Boltzmann constant, and T is the corresponding temperature)[31]. As presented in Supplementary Fig. S6 [13], there is negligable band shift in $BaAg_2As_2$ below the phase transition. If any, it is distinct from iron pnictides, but could be related with the δ~0.0052 structural distortion induced hopping parameter variation [32].

In $SrAg_4As_2$, another AgAs layered compound, Fermi surface reconstruction is speculated at the structural phase transition considering the discrepancy between the Fermi surface resolved by low temperature quantum oscillation experiments and DFT calculated Fermi surfaces with structural parameters at room temperature [11]. However, here our temperature-dependent ARPES study indicates that the phase transition in $BaAg_2As_2$ is not accompanied by Fermi surface reconstruction, but is an enhancement of dispersive spectral weight. It calls for future studies on other AgAs layered compounds to investigate whether they share the same transition nature as in $BaAg_2As_2$.

The spectral weight of dispersive bands represents the DOS of coherent carriers that have a significant influence on the resistivity. A change of DOS has been discovered in several materials [34–36]. In particular, in Nd-doped $La_{0.46}Sr_{0.54}MnO_3$ the increase of DOS near Fermi level is accompanied by a decrease in resistivity, similar to $BaAg_2As_2$ although the latter has no magnetism. Since the resistivity is directly related to the DOS of coherent carriers near Fermi level, the enhancement of dispersive spectral weight can be a possible reason why the resistivity drops below T_s. Such an enhancement may come from the increased coherence due to reduced scattering channels, or a different Ag-As hybridization condition, at the low temperature symmetry-breaking phase. Nevertheless, the mutual relation between structural transition and enhancement of dispersive DOS still calls for future theoretical explanations.

CONCLUSION

To summarize, we have performed systematic ARPES, synchrotron XRD and RSXS measurements on high-quality $BaAg_2As_2$ single crystals, and revealed their three dimensional electronic structure across their structural transition. A structural distortion was observed with $a \neq b$ distortion which solved the puzzle of why the tetragonal-type model no longer fits the diffraction data below the transition temperature [10]. Although the Fermi surfaces of $BaAg_2As_2$ satisfy nesting conditions, no diffraction peak of CDW order is observed at the nesting wave vectors. Moreover, neither the CDW gap nor band reconstruction is observed across the phase transition, excluding electronic-instability-induced CDW or orbital orders at low temperature. A significant enhancement on the spectral weight of dispersive features extending to -0.6 eV below the Fermi energy is observed across the structural phase transition, which can be related to the sharp drop of resistivity below the phase transition temperature. The weak response from the low energy electronic structure across the phase transition suggests the structural distortion in $BaAg_2As_2$ is not electronically instability driven, different from Fe-based superconductors. These studies help to understand the origin of the phase transition in $BaAg_2As_2$, which may also apply in other AgAs layered compounds.

ACKNOWLEDGEMENTS

We thank the Diamond Light Source for access to on beam line I05 (The proposal number is SI20697), the Shanghai Synchrotron Radiation Facility for access to beam line 9U, and the

Advanced Light Source for access to beam line 4.0.3. This work was supported by National Natural Science Foundation of China (Nos.11888101, 11704073, 11704074, 11922403, 11790310, U1532266), by the National Key R&D Program of the MOST of China (Grants Nos. 2016YFA0300200, 2017YFA0303004), and by Anhui Initiative in Quantum Information Technologies. Work at UCLA was supported by NSF DMREF program under the award NSF DMREF project DMR-1629457 and DMR-1435672. Part of research described in this paper was performed at the Canadian Light Source, which is supported by the Canada Foundation for Innovation, Natural Sciences and Engineering Research Council of Canada, the University of Saskatchewan, the Government of Saskatchewan, Western Economic Diversification Canada, the National Research Council Canada, and the Canadian Institutes of Health Research.

* Electronic address: pengrui@fudan.edu.cn

[1] Q. Huang, Y. Qiu, W. Bao, M. A. Green, J. W. Lynn, Y. C. Gasparovic, T. Wu, G. Wu, and X. H. Chen, Phys Rev Lett **101**, 257003 (2008).
[2] M. Rotter, M. Tegel, D. Johrendt, I. Schellenberg, W. Hermes, and R. Pottgen, Physical Review B **78**, 020503(R) (2008).
[3] X. Tan, Z. P. Tener, and M. Shatruk, Acc Chem Res **51**, 230 (2018).
[4] W. B. Jiang, C. Y. Guo, Z. F. Weng, Y. F. Wang, Y. H. Chen, Y. Chen, G. M. Pang, T. Shang, X. Lu, and H. Q. Yuan, J Phys Condens Matter **27**, 022202 (2015).
[5] K. Kudo, Y. Nishikubo, and M. Nohara, Journal of the Physical Society of Japan **79**, 123710 (2010).
[6] B. Zhou, M. Xu, Y. Zhang, G. Xu, C. He, L. X. Yang, F. Chen, B. P. Xie, X.-Y. Cui, M. Arita, K. Shimada, H. Namatame, M. Taniguchi, X. Dai, and D. L. Feng, Physical Review B **83**, 035110 (2011).
[7] L. X. Yang, B. P. Xie, Y. Zhang, C. He, Q. Q. Ge, X. F. Wang, X. H. Chen, M. Arita, J. Jiang, K. Shimada, M. Taniguchi, I. Vobornik, G. Rossi, J. P. Hu, D. H. Lu, Z. X. Shen, Z. Y. Lu, and D. L. Feng, Physical Review B **82**, 104519 (2010).
[8] M. Yi, D. H. Lu, J. G. Analytis, J. H. Chu, S. K. Mo, R. H. He, M. Hashimoto, R. G. Moore, I. I. Mazin, D. J. Singh, Z. Hussain, I. R. Fisher, and Z. X. Shen, Physical Review B **80**, 174510 (2009).
[9] R. M. Fernandes, A. V. Chubukov, and J. Schmalian, Nature Physics **10**, 97 (2014).
[10] S. S. Stoyko, P. E. R. Blanchard, and A. Mar, Journal of Solid State Chemistry **194**, 113 (2012).
[11] B. Shen, E. Emmanouilidou, X. Deng, A. McCollam, J. Xing, G. Kotliar, A. I. Coldea, and N. Ni, Physical Review B **98**, 235130 (2018).
[12] S. Bing, H. Chaowei, C. Huibo, G. Xin, E. Eve, X. Weiwei, and N. Ni, arXiv , 1809.07317v2 (2018).
[13] See Supplemental Material at [URL] for detailed information on resistivity measurements, the summary of doping level, Fermi surface mappings, MCP images of RSXS measurements, Hall resistivity measurements and comparisons of EDCs at Fermi crossings. .
[14] D. J. Singh, Physical Review B **79**, 153102 (2009).
[15] F. Massee, S. de Jong, Y. Huang, J. Kaas, E. van Heumen, J.B. Goedkoop, M.S. Golden, Physical Review B **80**, 140507(R) (2009).
[16] J. M. Luttinger, Physical Review **119**, 1153 (1960).
[17] R. E. Peierls, *Quantum theory of solids* (Clarendon Press, 1996).
[18] T. Nakagawa, G. I. Boishin, H. Fujioka, H. W. Yeom, I. Matsuda, N. Takagi, M. Nishijima, and T. Aruga, Phys Rev Lett **86**, 854 (2001).
[19] T. Pillo, J. Hayoz, H. Berger, M. Grioni, L. Schlapbach, and P. Aebi, Phys Rev Lett **83**, 3494 (1999).
[20] D. W. Shen, B. P. Xie, J. F. Zhao, L. X. Yang, L. Fang, J. Shi, R. H. He, D. H. Lu, H. H. Wen, and D. L. Feng, Phys Rev Lett **99**, 216404 (2007).
[21] K. McElroy, G. H. Gweon, S. Y. Zhou, J. Graf, S. Uchida, H. Eisaki, H. Takagi, T. Sasagawa, D. H. Lee, and A. Lanzara, Phys Rev Lett **96**, 067005 (2006).
[22] U. Chatterjee, M. Shi, A. Kaminski, A. Kanigel, H. M. Fretwell, K. Terashima, T. Takahashi, S. Rosenkranz, Z. Z. Li, H. Raffy, A. Santander-Syro, K. Kadowaki, M. R. Norman, M. Randeria, and J. C. Campuzano, Phys Rev Lett **96**, 107006 (2006).
[23] S.-K. Chan and V. Heine, Journal of Physics F: Metal Physics **3** (1973).
[24] D. S. Inosov, V. B. Zabolotnyy, D. V. Evtushinsky, A. A. Kordyuk, B. Bchner, R. Follath, H. Berger, and S. V. Borisenko, New Journal of Physics **10**, 125027 (2008).
[25] T. Pillo, J. Hayoz, H. Berger, M. Grioni, L. Schlapbach, and P. Aebi, Phys Rev Lett **83**, 3494 (1999).
[26] A. J. Achkar, X. Mao, C. McMahon, R. Sutarto, F. He, R. Liang, D. A. Bonn, W. N. Hardy, and D. G. Hawthorn, Phys Rev Lett **113**, 107002 (2014).
[27] P. Richard, K. Nakayama, T. Sato, M. Neupane, Y. M. Xu, J. H. Bowen, G. F. Chen, J. L. Luo, N. L. Wang, X. Dai, Z. Fang, H. Ding, and T. Takahashi, Phys Rev Lett **104**, 137001 (2010).
[28] Sergey L. Bud'ko, Xiaoming Ma, Milan Tomic, Sheng Ran, Roser Valenti, and Paul C. Canfield, Physical Review B **93**, 024516 (2016).
[29] A. Kreyssig, M. A. Green, Y. Lee, G. D. Samolyuk, P. Zajdel, J. W. Lynn, S. L. Budko, M. S. Torikachvili, N. Ni, S. Nandi, J. B. Leao, S. J. Poulton, D. N. Argyriou, B. N. Harmon, R. J. McQueeney, P. C. Canfield, and A. I. Goldman, Physical Review B **78**, 184517 (2008).
[30] J. Mansart, P. Le Fevre, F. Bertran, A. Forget, D. Colson, and V. Brouet, Physical Review B **94**, 235147 (2016).
[31] S. Tan,Y. Zhang,M. Xia,Z. Ye,F. Chen,X. Xie,R. Peng,D. Xu,Q. Fan,H. Xu,J. Jiang,T. Zhang,X. Lai,T. Xiang,J. Hu,B. Xie, and D. Feng, Nat Mater **12**, 634-40 (2013).
[32] W. A. Harrison, *Electronic Structure and the Properties of Solids: The Physics of the Chemical Bond* (Dover, New York, 1989).
[33] A. S. Sefat, M. A. McGuire, R. Jin, B. C. Sales, D. Mandrus, F. Ronning, E. D. Bauer, and Y. Mozharivskyj, Physical Review B **79**, 094508 (2009).
[34] T. Takeuchi, H. Nozaki, K. Soda, T. Kondo, U. Mizutani, Takayoshi, Yokoya, T. Sato, T. Takahashi, S. Shin, T. Muro, Y. Saitohe, and Y. Moritomof, J. Synchrotron Rad. **9**, 237 (2002).
[35] D. D. Sarma, N. Shanthi, S. R. Krishnakumar, T. Saitoh, T. Mizokawa, A. Sekiyama, K. Kobayashi, A. Fujimori, E. Weschke, R. Meier, G. Kaindl, Y. Takeda, and M. Takano, Phys Rev B **53**, 6873 (1996).
[36] J. Mitra, M. Paranjape, A. K. Raychaudhuri, N. D. Mathur, and M. G. Blamire, Physical Review B **71**, 094426 (2005).